Monthly Notices of the ROYAL ASTRONOMICAL SOCIETY LETTERS

Mon. Not. R. Astron. Soc. **423,** L35–L39 (2012) doi:10.1111/j.1745-3933.2012.01252.x

Improved collision strengths and line ratios for forbidden [O III] far-infrared and optical lines

Ethan Palay,[1] Sultana N. Nahar,[1] Anil K. Pradhan[1]★ and Werner Eissner[2]

[1]*Department of Astronomy, The Ohio State University, Columbus, OH 43210, USA*
[2]*Institut für Theoretische Physik, Teilinstitut 1, 70550 Stuttgart, Germany*

Accepted 2012 March 6. Received 2012 March 4; in original form 2011 December 5

ABSTRACT

Far-infrared and optical [O III] lines are useful temperature–density diagnostics of nebular as well as dust obscured astrophysical sources. Fine-structure transitions among the ground state levels $1s^2 2s^2 2p^3\ ^3P_{0,1,2}$ give rise to the 52- and 88-μm lines, whereas transitions among the $^3P_{0,1,2}$, $^1D_2$, $^1S_0$ levels yield the well-known optical lines λλ4363, 4959 and 5007 Å. These lines are excited primarily by electron impact excitation. However, despite their importance in nebular diagnostics collision strengths for the associated fine-structure transitions have not been computed taking full account of relativistic effects. We present Breit–Pauli *R*-matrix calculations for the collision strengths with highly resolved resonance structures. We find significant differences of up to 20 per cent in the Maxwellian averaged rate coefficients from previous works. We also tabulate these to lower temperatures down to 100 K to enable determination of physical conditions in cold dusty environments such photodissociation regions and ultraluminous infrared galaxies observed with the *Herschel Space Observatory*. We also examine the effect of improved collision strengths on temperature- and density-sensitive line ratios.

Key words: atomic data – atomic processes – line: formation – H II regions – planetary nebulae: general.

1 INTRODUCTION

[O III] optical lines have long been standard nebular temperature diagnostics with wavelengths almost in the middle of the optical spectrum at λλ4363, 4959, 5007 (see e.g. Aller 1956; Dopita & Sutherland 2003; Pradhan & Nahar 2011). In recent years, owing to the advent of far-infrared (FIR) space observatories and instruments such as the *Infrared Space Observatory* Long Wavelength Spectrograph (*ISO*-LWS), the *Spitzer* Infrared Spectrograph and the *Herschel* Photodetector Array Camera and Spectrometer (PACS), the [O III] FIR lines have proven to have great potential in providing diagnostics of physical conditions in a variety of astrophysical objects that are generally obscured by dust extinction at optical or shorter wavelengths. These range from Galactic H II regions (Martin-Hernandez et al. 2002; Morisset et al. 2002) to star-forming galaxies at intermediate redshift (Liu et al. 2008) and ultraluminous infrared galaxies (ULIRGs). For example, the [O III] FIR lines at λλ88 and 52 μm are observed from dusty ULIRGs, which are copious IR emitters and become more prominent with increasing redshift (Nagao et al. 2011). They may be valuable indicators of the metallicity evolution from otherwise inaccessible star-forming regions buried deep within the galaxies (Houck et al. 2004, 2005).

The forbidden FIR lines arise from very low energy excitations within the fine-structure levels of the ground state of atomic ions, such as the [O III] $^3P_0$–$^3P_1$ transition at 88.36 μm and the $^3P_1$–$^3P_2$ transition at 51.81 μm. As such, they can be excited by electron impact at low temperatures, even at $T_e \sim 1000$ K or less. That also accounts for their utility since the FIR lines can be formed in (and therefore probe) not only H II regions but also photodissociation regions where the temperature–density gradients are large (Nagao et al. 2011).

However, excitation of levels lying very close to each other implies that the associated cross-sections need to be computed with great accuracy at very low energies in order to yield reliable rate coefficients. The Maxwellian electron distribution at low temperatures samples only the near-threshold energies above the small excitation energy of the fine-structure transition. Relativistic fine-structure separations therefore assume special importance even for low-*Z* atomic ions in determining not only the energy separation but also the interaction of the incident electron with the target levels. Owing to its prominence in astrophysical spectra, a large number of previous studies have been carried out on electron impact excitation of O III (namely compilation of evaluated data by Pradhan & Zhang 2001). Among the recent ones, whose collision strengths are employed in astrophysical models, are Burke, Lennon & Seaton (1989),

★E-mail: pradhan.1@osu.edu

Aggarwal & Keenan (1999), and Crawford et al. (2000). However, these calculations are basically in *LS* coupling (Burke et al. 1989), or with intermediate coupling effects introduced perturbatively via an algebraic transformation from the *LS* to *LSJ* scheme (Aggarwal & Keenan 1999). Although the earlier calculations employed the coupled channel *R*-matrix method which takes account of the extensive resonance structures; the fine-structure separations are not considered. In this report we take account of both the resonances and fine structure in an ab initio manner.

Another recent development in relativistic *R*-matrix codes is the inclusion of the two-body fine-structure Breit interaction terms in the Breit–Pauli Hamiltonian (Nahar et al. 2011; Eissner & Chen, in preparation). A relativistic calculation of collision strengths can therefore be carried out, including fine structure explicitly and more accurately than in previous works. Relativistic effects are likely to be insignificant for optical transitions compared to the FIR transitions since the former involve relatively larger energy separations and relativistic corrections are small. Nevertheless, we consider all 10 forbidden transitions among the levels dominated by the ground configuration of O III.

2 THEORY AND COMPUTATIONS

A brief theoretical description of the calculations is given. In particular, we describe relativistic effects and the representation of the (e + ion) system.

2.1 Relativistic fine structure

The relativistic Hamiltonian (Rydberg units) in the Breit–Pauli *R*-matrix (BPRM) approximation is given by

$$H_{N+1}^{\rm BP} = \sum_{i=1}^{N+1}\left\{-\nabla_i^2 - \frac{2Z}{r_i} + \sum_{j>i}^{N+1}\frac{2}{r_{ij}}\right\} + H_{N+1}^{\rm mass} + H_{N+1}^{\rm Dar} + H_{N+1}^{\rm so}, \quad (1)$$

where the last three terms are, respectively, the following relativistic corrections:

$$\text{the mass correction term, } \mathrm{H^{mass}} = -\frac{\alpha^2}{4}\sum_{\rm i}\mathrm{p_i^4},$$

$$\text{the Darwin term, } H^{\rm Dar} = \frac{Z\alpha^2}{4}\sum_i \nabla^2\left(\frac{1}{r_i}\right),$$

$$\text{the spin–orbit interaction term, } H^{\rm so} = Z\alpha^2\sum_i \frac{1}{r_i^3}\boldsymbol{l}_i\cdot\boldsymbol{s}_i. \quad (2)$$

Equation (2) represents the one-body terms of the Breit interaction. In addition, another version of BPRM codes including the two-body terms of the Breit interaction (Nahar et al. 2011; Eissner & Chen, in preparation) has been developed, and is employed in the present work.

2.2 Effective collision strengths

Cross-sections or collision strengths at very low energies may be inordinately influenced by near-threshold resonances. Those, in turn, affect the effective collision strengths or rate coefficients computed by convolving the collision strengths over a Maxwellian function at a given electron temperature $T_{\rm e}$ as

$$\Upsilon_{ij}(T_{\rm e}) = \int_0^\infty \Omega_{ij}(\epsilon)\exp(-\epsilon/kT_{\rm e})\mathrm{d}(\epsilon/kT_{\rm e}), \quad (3)$$

where E_{ij} is the energy difference and Ω_{ij} is the collision strength for the transition *i*–*j*. The exponentially decaying Maxwellian factor implies that at low temperatures only the very low energy $\Omega_{ij}(E)$ would determine the $\Upsilon(T_{\rm e})$.

2.3 Wavefunction representation and calculations

Based on the coupled channel approximation, the *R*-matrix method (Burke et al. 1971; Berrington et al. 1995) entails a wavefunction expansion of the (e + ion) system in terms of the eigenfunctions for the target ion. In the present case we are interested in low-lying O/FIR transitions of the ground configuration $2s^22p^2$. Therefore, we confine ourselves to an accurate wavefunction representation for the first 19 levels dominated by the *spectroscopic* configurations $[1s^2]2s^22p^2$, $2s2p^3$, $2s^22p3s$. A much larger set of *correlation* configurations is included for configuration interaction with the spectroscopic terms using the atomic structure code SUPERSTRUCTURE (Eissner et al. 1974; Nahar et al. 2003): $[1s^2]2p^4$, $2s^22p3p$, $2s^22p3d$, $2s^22p4s$, $2s^22p4p$, $2s2p^23s$, $2s2p^23p$, $2s2p^23d$, $2s^23s^2$, $2s^23p^2$, $2s^23d^2$, $2s^24s^2$, $2s^24p^2$, $2s^23s3p$, $2s^23s4s$, $2s^23p3d$, $2p^33s$, $2p^33p$, $2p^33d$. We note here that the crucial fine-structure separations between the ground state $^3\mathrm{P}_{0,1,2}$ levels reproduced theoretically agree with experimentally measured values to ∼3 per cent (Nahar et al. 2011; see Pradhan & Nahar 2011, for a general description of atomic processes and calculations). The observed energies were substituted for theoretical ones in order to reproduce the threshold energies more accurately. This is of particular importance for excitation at low temperatures dominated by near-threshold resonances. Even though the observed and experimental values are close, a small difference in resonance positions relative to threshold can introduce a significant uncertainty in the effective collision strengths.

The collision strengths were computed employing the extended BPRM codes (Eissner & Chen 2012). Particular care is taken to test and ensure convergence of collision strengths with respect to partial waves and energy resolution. Total (e + ion) symmetries up to $(LS)J\pi$ with $J \leq 19.5$ and even/odd parities π were included in the calculations, though it was found that the collision strengths for all forbidden transitions converged for $J \leq 9.5$. An energy mesh of $\Delta E < 10^{-4}$ Rydberg was used to resolve the near-threshold resonances. The resonances were delineated in detail prior to averaging over the Maxwellian distribution.

3 RESULTS AND DISCUSSION

We describe the two main sets of results for the FIR and the optical transitions, as well as diagnostic line ratios.

3.1 Far-infrared transitions

The BPRM collision strengths for the two FIR fine-structure transitions 88, 52 μm are shown in Figs 1(a) and (b). Although the resonance structures look similar, the magnitude and energy variations are not the same. The Maxwellian averaged effective collision strengths $\Upsilon(T_{\rm e})$ are quite different, as shown in Fig. 2. While $\Upsilon(T_{\rm e};^3\mathrm{P}_0{-}^3\mathrm{P}_1)$ for the 88-μm transition is relatively constant over three orders of magnitude in temperature, the $\Upsilon(T;^3\mathrm{P}_1{-}^3\mathrm{P}_2)$ for the 52-μm transition varies by about a factor of 1.5 from the low-temperature limit of 100 K to temperatures $T_{\rm e} > 10\,000$ K. A comparison with the earlier work by Aggarwal & Keenan (1999) is shown as dashed lines, which range down to their lowest

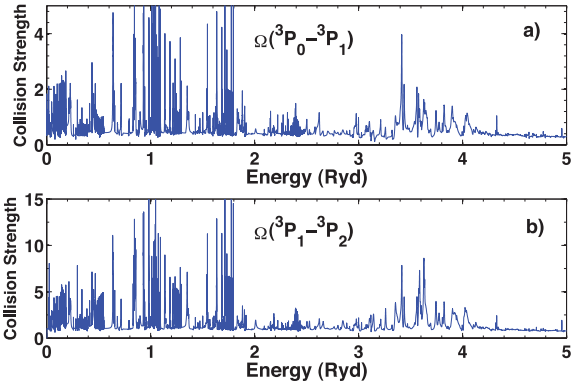

Figure 1. Collision strengths for the [O III] IR fine-structure transitions $2p^2(^3P_0–^3P_1, ^3P_1–^3P_2)$ at (a) 88 μm and (b) 52 μm, respectively. High resolution at near-threshold energies is necessary for accuracy in rate coefficients at low temperatures. The top panel shows an expanded view in the region $E \leq 1$ Rydberg; both transitions have similar resonance structures.

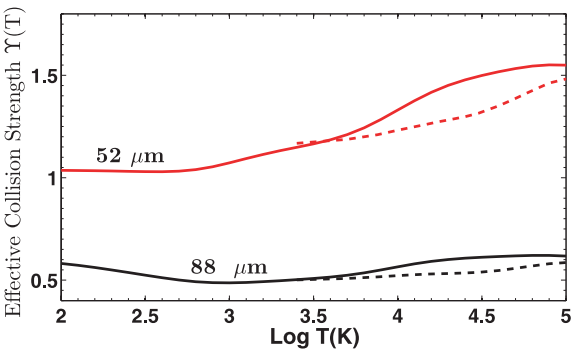

Figure 2. Maxwellian averaged effective collision strengths $\Upsilon(T_e)$ (equation 1) for the transitions $^3P_0–^3P_1$ at 88 μm and $^3P_1–^3P_2$ at 52 μm (solid lines; cf. Fig. 1). Previous results without relativistic effects (Aggarwal & Keenan 1999) are also shown (dashed lines) in the temperature range available $T_e \geq 2500$ K.

tabulated temperature 2500 K. It can be noted that if the Aggarwal and Keenan values are extrapolated linearly to lower temperatures, then one would obtain fairly constant effective collision strengths. However, the present results show marked difference owing to resonance structures as in Fig. 1.

Such temperature sensitivity of the otherwise density-sensitive 52/88 line ratio is illustrated in Figs 3(a) and (b). In Fig. 3(a) the solid lines are ratios with the present collision strengths, and the dashed lines are using previous results (Aggarwal & Keenan 1999). We find very good agreement, implying that at all temperatures down to 2500 K the differences in line ratios would be negligible. Fig. 3(b) shows the 52/88 ratio at various temperatures between 100 and 10 000 K. Whereas the ratio is relatively constant with density at 100 K, its dependence on density varies significantly with increasing temperature. The density–temperature diagnostic value of the 52/88 ratio is apparent from these curves. Therefore, care must be exercised to establish a temperature regime for the emitting region. Fig. 3(a) shows line ratios computed at 2500 and 10 000 K, and variations with electron density. It is also found that the values of line ratios at 2500 and 1000 K are very close together, implying convergence for $T_e \sim 1000$ K. Fig. 3(b) clearly demonstrates that the

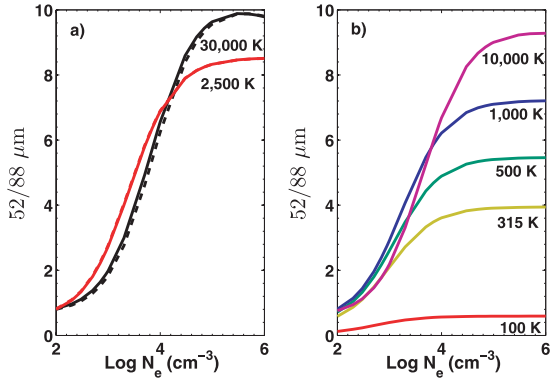

Figure 3. The density and temperature dependence of the 52/88 μm line ratios; (a) the solid curves are present results at 2500 and 30 000 K and the dashed lines are using the Aggarwal & Keenan (1999) effective collision strengths; (b) 52/88 ratio at temperatures $100 \leq T(\mathrm{K}) \leq 10000$.

line ratio decreases rapidly for $T < 1000$ K to almost flat at 100 K. The low-temperature regime 100–1000 K is therefore indicated by the curves shown in Fig. 3(b), as well as the limit where the 52/88 ratio is temperature invariant. Therefore, the 52/88 ratio is excellent density diagnostics in the typical density range $\log N_e \sim 3$–4 for $T_e > 1000$ K without much dependence on temperature (Fig. 3a). However, at lower temperatures the ratio may differ by up to a factor of 10 (Fig. 3b). Whereas the primary variations are owing to the exponential factors in $\Upsilon(T_e)$ (equation 3), we emphasize the role of relativistic fine-structure splitting between the $^3P_{0,1,2}$ levels and near-threshold resonances lying in between.

3.2 Forbidden optical transitions

Fig. 4 shows the collision strengths for the optical transitions $^3P_1–^1D_2$, $^3P_2–^1D_2$, $^1S_0–^1D_2$ at λλ4959, 5007, 4363, respectively. The effective collision strengths for the [O III] optical lines are shown in Fig. 5. These also differ significantly from previously available ones by up to 15 per cent. The new results are also obtained down to 100 K; their limiting values at low temperatures tend to 0.4:0.6:1.0. Since λλ4959, 5007 are often blended, it is common to plot the blended line ratio (4959+5007)/4363 shown in Fig. 6. This ratio

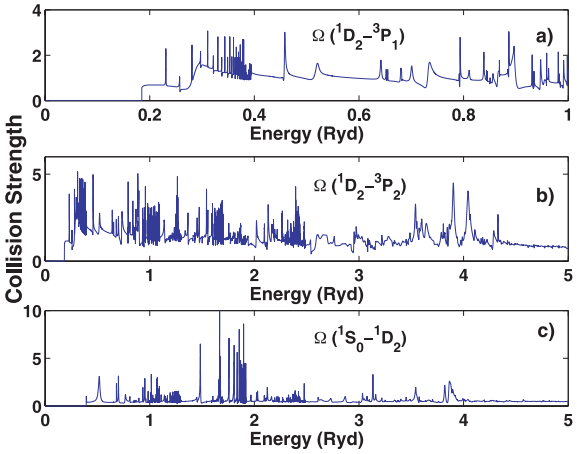

Figure 4. Collision strengths of the [O III] optical transitions. The two transitions $^1D_2–^3P_1$, $^1D_2–^3P_2$ in (a) and (b) have similar resonance structures; the top panel (a) presents an expanded view below $E \leq 1$ Rydberg.

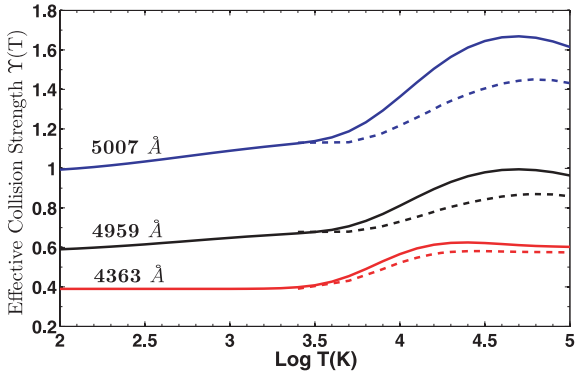

Figure 5. Effective collision strengths of the [O III] optical transitions $^1D_2$–$^3P_1$, $^1D_2$–$^3P_2$ and $^1S_0$–$^1D_2$ at λλ4959, 5007 and 4363, respectively (cf. Fig. 4).

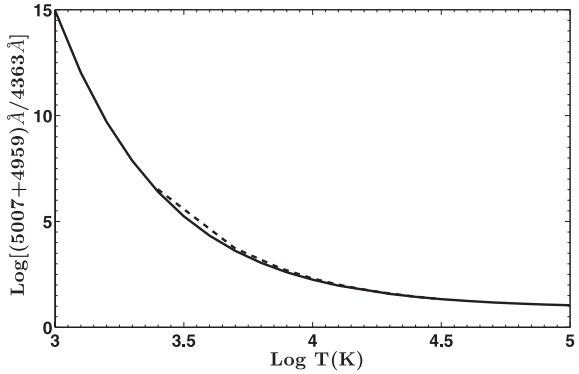

Figure 6. Blended [O III] line ratio (4959 + 5007)/4363 versus temperature, at $N_e = 10^3$ cm^{-3}. The dashed line using earlier data (Aggarwal & Keenan 1999) is plotted down to 2500 K.

varies over orders of magnitude since the uppermost $^1S_0$ level is far less excited at low energies than $^1D_2$, and therefore the level populations and line intensities depend drastically on temperature. A comparison is made with fine-structure collision strengths derived from the LS term values of Aggarwal & Keenan (1999) divided according to statistical weights, again shown as dashed lines in Figs 5 and 6. However, similar to Fig. 3(a), the differences in effective collision strengths do not translate into any significant differences in line ratios even at $\log T_e = 4.5$ (≈30 000 K) where the values differ most.

3.3 Maxwellian averaged collision strengths

In Table 1 we present the effective collision strengths (equation 3) for the 10 transitions among the ground configuration levels and their wavelengths. The tabulation is carried out at a range of temperatures typical of nebular environments, including the low-temperature range $T_e \leq 1000$ K not heretofore considered.

3.4 Conclusion

Improved collision strengths including fine structure with relativistic effects are computed. Owing to the diagnostic importance of the [O III] forbidden FIR and optical lines, the relatively small but significant differences of up to 20 per cent should provide more accurate line ratios. Particular attention is paid to the resolution of resonances in the very small energy region above threshold(s), enabling the study of low-temperature behaviour.

The line emissivities and ratios computed in this work demonstrate the temperature–density behaviour at low temperatures and at typical nebular temperatures. However, depending on the astrophysical sources, a complete model of line emissivities may also need to take into consideration the Bowen fluorescence mechanism: the *radiative* excitation of $2p^2\ ^3P_2$–$2p3d\ ^3P^0_2$ by He II Lyα at 304 Å and cascades into the upper levels of the forbidden transitions considered herein (see e.g. Saraph & Seaton 1980; Pradhan & Nahar 2011). In addition, for higher temperatures $T_e > 20\,000$ K proton impact excitation of the ground state fine-structure levels $^3P_{0,1,2}$ needs to be taken into account; at lower temperatures the excitation rate coefficient due to electrons far exceeds that due to protons (Ryans et al. 1999). Finally, there may be some contribution from (e + ion) recombination from O IV to [O III], since recombination rate coefficients increase sharply towards lower temperatures, while collisional excitation rates decrease (level-specific and total recombination rate coefficients may be obtained from S. N. Nahar's data base Nahar-OSU-Radiative-Data (NORAD) at www.astronomy.ohio-state.edu~nahar). Recombination contribution depends on the O IV/[O III] ionization fraction, which at low temperatures would be small.

ACKNOWLEDGMENTS

The computational work was carried out at the Ohio Supercomputer Center in Columbus Ohio. This work was partially supported by a grant from the NASA Astrophysical Research and Analysis programme. EP would like to gratefully acknowledge a Summer Undergraduate Research Programme grant from the Ohio State University.

Table 1. Effective Maxwellian averaged collision strengths.

Transition	λ	Υ(100)	Υ(500)	Υ(1000)	Υ(5000)	Υ(10 000)	Υ(20 000)	Υ(30 000)
$^3P_0$–$^3P_1$	88 μm	5.814(−1)	5.005(−1)	4.866(−1)	5.240(−1)	5.648(−1)	6.007(−1)	6.116(−1)
$^3P_2$–$^3P_0$	33 μm	2.142(−1)	2.153(−1)	2.234(−1)	2.469(−1)	2.766(−1)	3.106(−1)	3.264(−1)
$^3P_2$–$^3P_1$	52 μm	1.036(0)	1.032(0)	1.072(0)	1.210(0)	1.330(0)	1.451(0)	1.499(0)
$^1D_2$–$^3P_0$	4933 Å	1.959(−1)	2.088(−1)	2.154(−1)	2.347(−1)	2.693(−1)	3.094(−1)	3.256(−1)
$^1D_2$–$^3P_1$	4959 Å	5.903(−1)	6.285(−1)	6.483(−1)	7.067(−1)	8.108(−1)	9.313(−1)	9.802(−1)
$^1D_2$–$^3P_2$	5007 Å	9.934(−1)	1.056(0)	1.089(0)	1.188(0)	1.363 (0)	1.564(0)	1.645(0)
$^1S_0$–$^1D_2$	4363 Å	3.900(−1)	3.899(−1)	3.899(−1)	4.544(−1)	5.661(−1)	6.230(−1)	6.219(−1)
$^1S_0$–$^3P_1$	2321 Å	1.765(−1)	1.590(−1)	1.477(−1)	1.228(−1)	1.223(−1)	1.294(−1)	1.332(−1)
$^1S_0$–$^3P_2$	2332 Å	2.850(−1)	2.587(−1)	2.421(−1)	2.045(−1)	2.046(−1)	2.170(−1)	2.235(−1)
$^1S_0$–$^3P_0$	2317 Å	5.965(−2)	5.354(−2)	4.959(−2)	4.094(−2)	4.069(−2)	4.299(−2)	4.424(−2)

REFERENCES

Aggarwal K. M., Keenan F. P., 1999, ApJS, 123, 311
Aller L. H., 1956, Gaseous Nebulae. Wiley, New York
Berrington K. A., Eissner W., Norrington P. H., 1995, Comput. Phys. Commun., 92, 290
Burke P. G., Hibbert A., Robb W. D., 1971, J. Phys. B, 4, 153
Burke V. M., Lennon D. J., Seaton M. J., 1989, MNRAS, 236, 353
Crawford F. J., Keenan F. P., Aggarwal K. M., Wickstead A. W., Aller L. H., Feibelman W. A., 2000, A&A, 362, 730
Dopita M. A., Sutherland R. S., 2003, Astrophysics of the Diffuse Universe. Springer-Verlag, Berlin
Eissner W., Jones M., Nussbaumer H., 1974, Comput. Phys. Commun., 8, 270
Houck J. R. et al., 2004, ApJS, 154, 18
Houck J. R. et al., 2005, ApJ, 622, L105
Liu X., Shapley A. E., Coil A. L., Brenchmann J., Ma C.-P., 2008, ApJ, 678, 758
Martin-Hernandez et al., 2002, A&A, 381, 606
Morisset C., Schaerer D., Martin-Hernandez N. L., Peeters E., Damour F., Baluteau J.-P., Cox P., Roelfsema P., 2002, A&A, 386, 558
Nagao T., Maiolino R., Marconi A., Matsuhara H., 2011, A&A, 526, A149
Nahar S. N., Eissner W., Chen G.-X., Pradhan A. K., 2003, A&A, 408, 789
Nahar S. N., Pradhan A. K., Montenegro M., Eissner W., 2011, Phys. Rev. A, 83, 053417
Pradhan A. K., Nahar S. N., 2011, Atomic Astrophysics and Spectroscopy. Cambridge Univ. Press, Cambridge
Pradhan A. K., Zhang H. L., 2001, in Itikawa Y., ed., Landolt-Börnstein Vol. 17, Photon and Electron Interactions with Atoms, Molecules, Ions. Springer-Verlag, Berlin, p. 1
Ryans R. S. I., Foster-Woods V. J., Reid R. H. G., Keenan F. P., 1999, A&A, 345, 663
Saraph H. E., Seaton M. J., 1980, MNRAS, 193, 617

This paper has been typeset from a TEX/LATEX file prepared by the author.